Determining Physical Properties of Unconventional Reservoir Rocks: from Laboratory Methods to Pore-Scale Modeling

CONFERENCE PAPER · NOVEMBER 2013

DOI: 10.2118/167058-MS

Dirk Mallants
The Commonwealth Scientific and Industri…

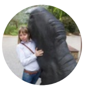

Marina Vladimirovna Karsanina
Russian Academy of Sciences

Kirill Gerke
University of Melbourne

SPE 167058-MS

Determining Physical Properties of Unconventional Reservoir Rocks: from Laboratory Methods to Pore-Scale Modeling

Kirill M. Gerke, CSIRO Land and Water; Roman V. Vasilyev, Geology Faculty of Lomosnosov Moscow State University, AIR Technology; Dmitry V. Korost, Geology Faculty of Lomosnosov Moscow State University; Marina V. Karsanina, Institute of Geopsheres Dynamics of Russian Academy of Sciences , AIR Technology ; Natalya S. Balushkina, Ruslan Khamidullin, Georgy A. Kalmykov, Geology Faculty of Lomosnosov Moscow State University; Dirk Mallants, CSIRO Land and Water

This paper was prepared for presentation at the SPE Unconventional Resources Conference and Exhibition-Asia Pacific held in Brisbane, Australia, 11–13 November 2013.

Abstract

With the rapid progress of imaging methods it is now possible to obtain detailed rock structure information on different scales, ranging from nanometers to micrometers. Such knowledge facilitates use of pore-scale modeling approaches to predict numerous physical properties based on three dimensional structural data. Pore-scale modeling approaches can simulate different processes in the rock under natural conditions (pressure, temperature, etc.), which are more difficult to simulate in the laboratory. This is especially important for unconventional reservoir rocks such as the Bazhen formation siliceous rocks (black shales) used in this study. Based on X-ray microtomography and SEM imaging we develop a detailed categorization of different types of porosities (including micro, i.e. larger than μm size, and nano, i.e. sub-micron size, porosities) for samples of Bazhen siliceous rocks. Standard pore-scale modeling techniques do not account for different flow regimes within different pore sizes. Thus, we develop a pore-network model with different physics of gas flow for micro- and nanoporosity. High-resolution images are used for stochastic reconstructions of 3D structure and subsequently used for modeling of gas permeability. Resulting permeability values are in a good agreement with gas permeabilities measured for Bazhenov siliceous rocks. Finally, we present a framework to model gas permeability of unconventional reservoir rocks using multi-scale 3D structure information based on microCT scans and high resolution SEM/FIB-SEM imaging techniques.

Nomenclature

V_{ij} – flow rate from i-th to j-th element of a network model, m^3/s

r_{ij} – characteristic radius of channel between i-th and j-th elements, m

μ – fluid viscosity, Pa·s

Δp_{ij} – pressure difference between i-th and j-th elements, Pa

S –cross-section area, m^2

L –length, m

M – molar mass of gas, kg/mol

R – universal gas constant, J/(K·mol)

T – temperature, K

$\langle p \rangle$ – average pressure, Pa

$\langle \rho \rangle$ – average fluid density, kg/m^3

α - tangential momentum accommodation coefficient, dimensionless

P – cross-section perimeter, m

q_{ij} – volumetric conductance of unit-length channel with cross-section such as between i-th and j-th elements, $m^4/(Pa\cdot s)$

R – flow resistivity, $Pa\cdot s/m^3$

C_{ij} – flow conductance between i-th and j-th elements, $m^3/(Pa\cdot s)$

Q – total volumetric flow rate, m^3/s

Q_{in} – total inlet volumetric flow rate, m^3/s

Q_{out} - total outlet volumetric flow rate, m^3/s
$Adj(i)$ – set of network elements adjacent to the i-th
k_P – permeability, m^2
p – local pressure, Pa
$I^{(i)}$ - indicator function for binarized media, either 0 or 1
f_n^α - sets of correlation functions calculated before and after permutation during simulated annealing
P – probability of the permutation during simulated annealing, dimensionless
E, E_{new}, E_{old} – differences between correlation functions for two given states during simulated annealing, dimensionless
k– number of permutations
λ – parameter of simulated annealing cooling schedule

Introduction

Developing geological survey products and large-scale reservoir models requires detailed information on reservoir rock properties. Such information typically includes grain size distribution, absolute and relative permeabilities, formation factor, and residual oil/water content. The only available method to study these properties in a direct way is by means of laboratory analysis of core material. However, almost all unconventional reservoirs (shales, tight sands, etc.) are known for their extremely high formation pressures, while they usually have been developed for resource extraction using horizontal wells which makes core extraction virtually impossible. Even if some core material is obtained from the reservoirs, only porosity measurements using such techniques as NMR and mercury porosimetry are applicable to porous spaces filled with kerogen and bitumen. For porosity measurements these organic materials should be extracted first (usually by dissolution), a process which often results in sample destruction as some fraction of the organics is also part of the matrix (i.e. the non-extractable fraction during production). Unlike core material, drilling cuts are almost always available for analysis and can be readily processed in the laboratory. Numerous laboratory and semi-analytical methods for gas permeability measurements on drilling cuts have been developed, but they all share the disadvantages of conventional laboratory approaches, especially for rocks initially filled with hydrocarbons (as Bazhenov siliceous rock which we use as an example in this study).

In recent years different pore-scale modeling methods based on 3D pore structure information were proven to be valuable tools in determining numerous rock physical properties; X-ray microtomography (Blunt et al., 2013) was usually used to obtain microstructural data. However, the latter method has some prominent limitations, namely 1) resolution limits resulting in so-called under-resolution porosity, 2) trade-off between resolution and sample size, 3) difficulties in segmentation for materials (or phases) with similar densities due to similar x-ray absorption coefficients. Under-resolution porosity is manitested for many rock types, and can even affect modeling results for sandstone samples (Korost and Gerke, 2012). These limitations make it very difficult to only use microtomography for generating pore structure information for pore-scale modeling of unconventional reservoir rocks. Moreover, the latter are usually a complex mixture of organics, minerals and clay where matrix porosity is mainly represented by nano-size pores. A potentially more appropriate method to study sub-micron porosity is through very-high resolution Focused Ion Beam-Scanning Electron Microscopy (FIB-SEM) (Ambrose et al., 2012; Dewers et al., 2012). This technique has the disadvantage of being very time consuming and its analysis is further material dependent. In other words, there is no single laboratory analysis method for obtaining detailed pore structure information for every type of porosity typical of porous materials from unconventional reservoirs.

Use of pore-scale models for coupling of detailed information on pore structure obtained from different scales important for flow, e.g., micro (down to micron scale) and nano-porosity (down to 10 nm), offers an elegant way to link different physics of flow with each porosity domain and solve for permeability (Mehmani et al., 2013). Another important advantage of the pore-scale modeling approach is the simplicity with which simulation conditions can be changed, e.g. temperature, pressure, number of flowing fluids, or even dynamic structure changes due to crack formation induced by pressure changes. Such an approach can also be used to study through simulation matrix desorption and outflow of hydrocarbons (e.g. methane) due to reservoir depressurization, and thus estimate productivity rates and its dynamics. Current limitations to productivity assessment of unconventional reservoirs include lack of a versatile framework for assessing their properties using pore-scale modeling approaches, the absence of robust solutions for multi-scale multi-phase flow problems and lack of experience in applying 3D pore structure acquiring methods for micro and nano-porosity.

The objective of this paper is to develop a framework for determining unconventional reservoir rock properties using 3D pore-scale models build from the porous structure of cores or drilling cuts. To this end, we combine i) detailed laboratory measurements of physical properties (permeability and porosity) on more than 50 samples of black shales, ii) our previously developed concept of under-resolution porosity (Korost and Gerke, 2012), iii) X-ray microtomography scans and SEM images for these samples, and iv) pore-network modeling of their flow and transport properties using different physics for micro- and nanopores.

Materials and methods

Bazhen formation and samples

Bazhenov siliceous rocks are probably the most studied unconventional reservoir in Western Syberia (Braduchan et al., 1986). Its basin has an area of more than 1 million km^2 and layer thickness ranging from 10 to 100 m (with average value of 60 m). This type of shales is usually called black shales and filled with bitumen and other organic material. Overall estimated extractable amount of hydrocarbons vary from 0.6×10^9 to 30×10^9 tons (Kalmykov et al., 2010); this uncertainty in hydrocarbon yield is mainly due to the inability to predict Bazhen formation properties and their spatial variability. As a result of heterogeneity, the productivity can differ orders of magnitude for wells located closed to each other. Detailed studies on unperturbed rock samples are limited because of the difficulty to extract core material and risks of disturbance during extraction.

To develop a framework for accessing physical properties of unconventional reservoirs using laboratory methods and pore-scale modeling we selected more than 50 core samples of Bazhenov siliceous rock from an approximate depth of 2 km (Khamidullin et al, 2012).

Sample processing and laboratory measurements

Gas porosity was measured using a Coretest AP-608 device under atmospheric and pressurized conditions (pore pressure of 1.38 MPa) and four different swaging pressures of 3.45, 10, 20 and 30 MPa. Nitrogen gas was used and 12 measurements for each sample were performed for the five pressure conditions and an average value was reported based on all 12 measurements.

Porosity and permeability measurements for Bazhenov siliceous rock using conventional techniques usually result in highly overestimated values due to the fact that organic matter is part of the matrix and removing organic matter may destroy the integrity of the matrix. In some cases after chemical extraction of the organic matter, the core material is falling apart with no possibility of any further measurements. Previous studies have shown that most trustful porosity values are obtained by kerosene saturation without chemical extraction (Khamidullin et al, 2012).

Imaging

All samples were scanned using a Skyscan-1772 X-ray microtomography device with resolution of 1 µm. Scanning electron microscope was used to study submicron porosity.

SEM imaging of shales without milling with FIB or Broad Ion Beam (BIB) devices results in so-called 2.5D structures. For further analysis and stochastic reconstructions segmented 2D cuts are needed (i.e., binarized images with pore and solid material phases). To perform such a segmentation we used a two-step approach, i.e. first indicator kriging (Oh and Lindquist, 1999) to binarize the image followed by stereographic algorithms (Sergeev et al., 1984).

Reconstructions

There are many types of spatial correlation function functions available for image reconstruction (n-point probability, linear, cluster, chord, pore-size, etc.) (Torquato, 2002). For illustration purposes, let us consider the most important and well studied n-point probability function that defines the probability that n points are found in the same phase (in our case, either solids or pore space):

$$S_n^{(i)}(\vec{x}_1,\vec{x}_2,...,\vec{x}_n)=\left\langle I^{(i)}(\vec{x}_1)I^{(i)}(\vec{x}_2)...I^{(i)}(\vec{x}_n)\right\rangle \quad (1)$$

where x is a vector component, and I is the indicator function for binary systems (*i*=1,2) defined as:

$$I^{(i)}(\vec{x})=\begin{cases}1,\vec{x}\in V_i\\ 0,\vec{x}\in \overline{V_i}\end{cases} \quad (2)$$

The two-point probability function can be written as:

$$S_2^{(i)}(\vec{x}_1,\vec{x}_2)=\left\langle I^{(i)}(\vec{x}_1)I^{(i)}(\vec{x}_2)\right\rangle \quad (3)$$

For any number of correlation functions (Yeong and Torquato, 1998):

$$E=\sum_{\vec{r}_1,\vec{r}_2,...,\vec{r}_n}\sum_{\alpha}[f_n^{\alpha}(\vec{r}_1,\vec{r}_2,...\vec{r}_n)-\hat{f}_n^{\alpha}(\vec{r}_1,\vec{r}_2,...\vec{r}_n)]^2 \quad (4)$$

Pixels/voxels are randomly interchanged to achieve a target function, exchange is accepted using the energy concept:

$$P(E_{old}\rightarrow E_{new})=\begin{cases}1,\Delta E<0\\ \exp(-\Delta E/T),\Delta E\geq 0\end{cases} \quad (5)$$

$$\Delta E=E_{new}-E_{old} \quad (6)$$

Following cooling schedule was utilized:

$$T(k)/T(0)=\lambda^k \quad (7)$$

For example, applying equation (4) for two-point probability function will yield:

$$E = \sum_{i} [S_2(r_i) - \hat{S}_2(r_i)]^2 \quad (8)$$

We implement three different types of reconstruction based on modified Yeong-Torquato technique: 1) using averaged two-point probability function S_2, 2) same S_2 functions, but computed in directions (S_{2xyz}), 3) and, finally, a two-point probability function and linear functions (SL_{2xyz}) computed in directions. All reconstructions were performed from binarized images of porous structures to 3D images with volumes of 300^3 voxels. We used the voxel permutation acceleration method developed by Capek et al. (2011), where the maximal length of calculated correlation functions during reconstruction was 120 pixels, λ=0.999.

In total we have reconstructed nine 3D images from three 2D binarized cuts (Images 1-3) obtained from SEM images (Fig.6).

Pore-scale modeling

Pore-network models are used to assess the gas permeability of reconstructed 3D images (Blunt et al., 2002). We distinguish the mode of the fluid flow process (i.e. Hagen-Poiseuille or Knudsen diffusion) depending on pore or throat radius and assume it to be Hagen-Poiseuille (for microscale porosity) or Knudsen (for nanoscale porosity) based on a radius threshold value (e.g., radius is smaller than 1 μm). In case of the microscale mode, we use the Hagen-Poiseuille equation to describe the volumetric flow rate through a single pore network element:

$$V_{ij} = \frac{\pi r_{ij}^4}{8\mu} \cdot \frac{\Delta p_{ij}}{L} = \frac{S r_{ij}^2}{8\mu} \cdot \frac{\Delta p_{ij}}{L}. \quad (9)$$

The nanoscale flow approach is based on the Knudsen gas transport equation, for which the volumetric flow rate is equal to (Mehmani et al., 2013):

$$V_{ij} = \left[\frac{2M r_{ij}}{3 \cdot 10^3 RT} \sqrt{\frac{10^3 RT}{\pi M}} + \left(1 + \frac{\mu \left({}^{2}/_{\alpha} - 1 \right)}{\langle p \rangle r_{ij}} \sqrt{\frac{8 \cdot 10^3 \pi RT}{M}} \right) \frac{\langle \rho \rangle r_{ij}^2}{8\mu} \right] \frac{S \Delta p_{ij}}{\langle \rho \rangle L}. \quad (10)$$

There are three types of cross-sectional shapes of network elements for pores and throats in our pore network model: circular, square and triangular. For the last two cross-section types some equivalent radius r_{ij} should be inputted in equations (9) and (10). We determine this quantity as function of the cross-sectional shape properties perimeter and area (Mason and Marrow, 1991). For a triangular shape we assume:

$$r_{ij} = \sqrt{\frac{24}{5} \frac{S}{P}}, \quad (11)$$

and for a square shape:

$$r_{ij} = \sqrt{8 \cdot 0.5623} \frac{S}{P}. \quad (12)$$

This approach is based on the common Hagen-Poiseuille formula (Valvatne and Blunt, 2004):

$$q_{ij} = k \frac{S^3}{\mu P^2}, \quad (13)$$

where k = 0.5, 0.6 and 0.5623 for circular, triangular and square cross-sectional shapes respectively (Patzek and Silin, 2001).

To compute permeability of the entire pore network the system of equations containing pressures as unknowns must be solved. Each equation means a flow balance for one certain pore: total volumetric flow rate through interior pores is equal to zero and equal to inlet/outlet flow rate for the ones connected directly outside. First, flow resistances between adjacent pore network elements are computed:

$$R_{1,2} = \left(\frac{V_{1,2}}{\Delta p_{1,2}} \right)^{-1}. \quad (14)$$

Then flow resistance between the i-th and j-th pores are obtained as algebraic sum:

$$R_{ij} = R_{p1,t} + R_t + R_{t,p2} \quad (15)$$

Followed by the pore-to-pore volumetric conductance:

$$C_{ij} = \frac{1}{R_{ij}}. \quad (16)$$

Thus, pore-to-pore flow rate can be found as:

$$V_{ij} = C_{ij} \Delta p_{ij}. \quad (17)$$

The balance equation for a single pore is:

$$\sum_{j \in Adj(i)} V_{ij} = \sum_{j \in Adj(i)} C_{ij} (p_i - p_j) = 0, \quad (18)$$

where $A_{dj}(i)$ is a set of pores directly connected to the i-th one.

Since the system of equations like (18) for each pore is resolved, pressure amounts within all pores are known. Then the volumetric flow rate through the entire network can be computed in the following way:

$$Q = \frac{1}{2}(Q_{in} + Q_{out}) = \frac{1}{2}\left(\sum_{j\in I} C_{ij}(p_I - p_j) + \sum_{j\in O} C_{ij}(p_j - p_O)\right). \quad (19)$$

The set of pores directly connected to inlets is I and the ones connected to outlets is O, p_I and p_O are the inlet and outlet pressures respectively. Absolute permeability is obtained from Darcy's law:

$$k_P = \frac{Q\mu L}{S(p_O - p_I)}. \quad (20)$$

But as it can be noticed, equation (10) is non-linear on the pressure difference between pore network elements. To solve system of such equations the Newton method is used. Consider the following mapping:

$$\boldsymbol{Q}(\boldsymbol{p}) = \left(q_1(\boldsymbol{p}), q_2(\boldsymbol{p}), \dots, q_N(\boldsymbol{p})\right), \quad (21)$$

where $q_i(\boldsymbol{p})$ denotes the total flow through i-th pore, $\boldsymbol{p} = (p_1, p_2, \dots, p_N)$ is a vector of pressures in all of the pores, N is the number of pores. Due to the fluid flow balance

$$q_i(\boldsymbol{p}) = \sum_{j\in Adj(i)} C_{ij}\left(p_i - p_j\right) = 0, i = \overline{1, N}. \quad (22)$$

We then apply Newton's method using the solution $\boldsymbol{p}_{\boldsymbol{linear}}$ of the linear problem $\boldsymbol{Q}(\boldsymbol{p}) = \boldsymbol{0}$ as a first approach, where C_{ij} is expressed from equations (9) and (17). The recurrent formula of the iterative process is as follows:

$$\boldsymbol{p}_{i+1} = \beta \boldsymbol{J}_{\boldsymbol{Q}}^{-\boldsymbol{1}}\left(\boldsymbol{J}_{\boldsymbol{Q}}(\boldsymbol{p}_i)\boldsymbol{p}_i - \boldsymbol{Q}(\boldsymbol{p}_i)\right) + (1 - \beta)\boldsymbol{p}_i, \quad (23)$$

where $\boldsymbol{J}_{\boldsymbol{Q}}$ denotes the jacobian of mapping $\boldsymbol{Q}(\boldsymbol{p})$ and $\beta = 0.9$ is a smoothing coefficient. Elements of jacobian are:

$$\frac{\partial q_i}{\partial p_j} = \begin{cases} \sum_{k\in Adj(i)} \left[C_{ik} + (p_i - p_k)\frac{\partial C_{ik}}{\partial p_i}\right], j = i \\ \left(p_i - p_j\right)\frac{\partial C_{ij}}{\partial p_j} - C_{ij}, j \in Adj(i) \\ 0, \ \ j \notin Adj(i) \cup \{i\} \end{cases} \quad (24)$$

Derivatives of conductance by pressure are:

$$\frac{\partial C_{ij}}{\partial p_i} = -C_{ij}^2 \rho(\varphi_{1i} + \omega_i), \quad (25)$$

$$\frac{\partial C_{ij}}{\partial p_j} = -C_{ij}^2 \rho\left(\omega_j + \varphi_{2j}\right) \quad (26)$$

Amounts ω and φ depend of micro- or nanoscale of a certain throat and pore respectively and in case of microscale they are equal to zero because C_{ij} does not depend on pressure. However, in case of nanoscale

$$\varphi_{1i} = \frac{ABr_{p1}L_{p1}}{p_i^2 U_{p1}^2 S_{p1}}; \ \varphi_{2j} = \frac{ABr_{p2}L_{p2}}{p_j^2 U_{p2}^2 S_{p2}}; \ \omega_i = \frac{L_t}{U_t^2 S_t} \cdot \frac{2ABr_t\left(1 + p_j\right)}{\left(p_i + p_j\right)^2}; \omega_j = \frac{L_t}{U_t^2 S_t} \cdot \frac{2ABr_t(1 + p_i)}{\left(p_i + p_j\right)^2}. \quad (27)$$

In these expressions, U means the mass conductance between pores and throats:

$$U_{1,2} = \frac{L_{1,2}\rho}{R_{1,2}S}, \quad (28)$$

$$A = \frac{\rho}{8\mu}, B = \mu\left(\frac{2}{\alpha} - 1\right)\sqrt{\frac{8 \cdot 10^3 \pi RT}{M}}. \quad (29)$$

All pore-networks are extracted from 3D images using the maximal inscribed ball algorithm (Silin and Patzek,2001; Dong and Blunt, 2009). All calculations are made assuming room temperature conditions and nitrogen gas.

Results and discussion

Main mineral and physical properties for the samples are shown in Table 1. It is still not clear to what extend kerosene saturation and chemical extraction can remove bitumen and other organics and, thus, affect permeability. It can be argued, that any disturbance as a result of processing the samples in the laboratory can cause significant changes in internal structure of the sample. Permeability determination methods that do not alter the pore structure such as pore-scale modeling, present a valuable alternative to the more destructive laboratory measurements.

High-resolution SEM imaging clearly showed presence of kerogen porosity, which was also found previously in many other shales (Loucks et al., 2009; Curtis et al., 2010), but not in Bazhenov siliceous rocks. Figure 1 (top) shows SEM images with visible sponge-like porosity at different resolutions, while spatial distribution of sulphur (blue), carbon (green) and silicon (red) is displayed in Figure 1 (bottom). The main reason to visualize the elements S, C, and Si is determined by their linkage to minerals' composition: silicon can be used as a tracer for biogenic silica and clays (biogenic silica is visible in the lower right part with a much more intense red due to higher silicon content while clay minerals are present as lighter red in the upper left part), sulfur indicates presence of pyrite, while carbon represents kerogen distribution (due to vacuum conditions applied during the SEM imaging all free hydrocarbons otherwise present in the rock evaporate). Analysis of numerous SEM images demonstrates that circular and oval pores shown in Figure 1 make up the porosity attributable to kerogen; such porosity is very abundant in Bazhenov siliceous rocks and contributes up to 30 % of total porosity.

Table 1. Measured mineral composition and physical properties for Bazhenov shales.

	Physical properties		**Mineral composition, %**								
Sample	Gas permeability, mD	Porosity, %	Quartz, %	Clay minerals,%	Carbonates, %	Dolomite, %	Calcite, %	Organic matter, %	Pyrite, %	Na/Feldspar, %	Siderite, %
1	2.56	9.45	58.50	15.37	4.26	2.95	1.31	12.16	1.74	5.85	2.12
2	0.07	6.98									
3	0.01	6.29	83.24	4.99	2.24	1.00	1.24	16.02	4.48	5.58	0.00
4	<0,01	7.12									
5	<0,01	6.10	70.44	11.01	3.10	0.00	3.10	8.80	3.10	3.55	0.00
6	0.01	4.25	60.24	17.33	1.96	1.96	0.00	13.37	2.47	4.63	0.00
7	<0,01	4.56	58.78	20.14	2.18	2.18	0.00	11.90	2.06	4.93	0.00
8	<0,01	5.34	67.04	15.29	1.28	0.00	1.28	9.47	3.42	3.50	0.00
9	0.02	3.67	32.44	5.07	43.93	43.93	0.00	0.00	17.01	1.55	0.00
10	1.87	5.65	29.71	3.10	44.51	44.51	0.00	5.99	15.59	1.09	0.00
11	2.55	6.64	65.07	13.70	1.24	0.00	1.24	11.41	5.77	2.81	0.00
12	0.02	4.28									
13	0.18	2.97	62.08	16.57	1.19	1.19	0.00	11.58	4.27	4.31	0.00
14	<0,01	3.64	62.34	16.58	1.51	1.51	0.00	11.14	3.83	4.60	0.00
15	1.81	2.52									
16	0.01	3.21	45.20	28.16	5.79	2.21	3.57	9.20	5.88	5.79	0.00
17	<0,01	4.87	55.58	14.08	10.33	8.37	1.96	10.77	4.77	4.46	0.00
18	0.03	3.99	40.84	18.16	16.11	16.11	0.00	8.71	11.25	4.94	0.00
19	---	4.72	40.24	12.55	32.10	17.77	14.34	4.82	6.38	3.90	0.00
20	---	3.31									
21	0.01	4.28	56.37	10.07	13.33	7.56	5.77	10.76	3.09	4.71	1.67
22	0.01	6.88	71.26	9.06	7.72	7.72	0.00	7.01	0.79	3.36	0.80
23	0.17	8.40	49.55	12.18	6.12	3.21	2.91	17.24	6.17	4.37	4.37
24	0.13	6.73	61.31	11.34	7.56	7.56	0.00	8.00	4.71	3.95	3.13
25	0.05	9.07	64.83	10.53	1.35	1.35	0.00	15.79	2.49	3.21	1.80
26	0.00	2.47	23.88	14.79	41.67	25.61	16.06	4.88	4.94	9.09	0.76
27	0.04	5.57	19.53	9.89	49.97	23.31	26.66	8.37	5.17	7.07	0.00
28	0.07	7.66	30.70	13.94	32.91	3.78	29.13	9.77	6.59	5.27	0.81
29	0.25	5.35	24.88	24.38	22.28	5.79	16.49	10.09	6.76	9.35	2.27
30	0.07	8.44	89.60	4.80		0.00	0.00		3.70	1.70	0.20
31	0.08	8.72									
32	0.05	7.83									
33	0.05	7.37	85.80	4.70		0.00	0.00		6.30	1.70	1.50

34	1.17	4.35	52.20	1.30		42.90	0.00		3.60	0.00	0.00
35	0.17	7.06	56.30	7.40		26.40	4.00		3.90	1.90	0.00
36	51.35	15.17									
37	2.94	12.40									
38	1.93	12.11	67.10	4.50		22.60	0.20		4.70	0.50	0.40
39	3.00	10.99	76.10	1.60		16.70	0.20		4.90	0.40	0.00
40	2.38	11.90	77.20	3.00		10.80	0.00		8.60	0.40	0.00
41	2.66	11.67	61.90	5.40		16.90	6.50		8.30	1.00	0.00
42	0.05	4.81	76.80			1.40	21.00		0.80	0.00	0.00
43	0.02	0.09	48.70	1.40		44.80	0.40		4.60	0.00	0.00
44	0.06	0.95	1.00	0.00		0.40	96.20		2.40	0.00	0.00
45	0.02	0.57	12.10	0.00		0.00	86.60		1.30	0.00	0.00
46	0.58	1.47	49.80	0.00		0.00	49.80		0.40	0.00	0.00
47	0.05	4.81	76.80	0.00		1.40	21.00		0.80	0.00	0.00

🟦	Micro and mineral nano-porosity
🟩	Mineral and kerogen nano-porosity
⬜	Micro, mineral and kerogen nano-porosity

High-resolution (1 µm resolution) microtomography imaging showed (Figure 2-4) that the main porosity in Bazhenov siliceous rocks is attributed to amorphous organic matter or voids filled with free hydrocarbons and probably kerogen, there are no cracks or fissures and there is no evidence for clay layering. Attenuation coefficients are different for certain types of organic compounds, therefore it is impossible to distinguish between pores and mixtures of kerogen and bitumen. The image analysis resulted into two subtypes of organic compounds associated with different pores: the first type is the least dense material (i.e. hydrocarbons) occupying large pores (larger than 1 µm), while the second type is all other amorphous organics, mainly kerogen. Clearly, hydrocarbon-containing large pores do not seem to be connected, while pores filled with kerogen form a well connected network in all samples (Figure 2-4). Usually, the following main phases can be distinguished on microtomography scans: 1) large pores 2) mixture of organics (including kerogen), 3) pyrite, and 4) rock matrix mainly composed of siliceous materials. In addition, Figure 2 shows a combination of different phases in a larger scale (image width is 100 µm) to highlight connectedness/disconnectedness among phases.

Combination of X-ray microtomography and SEM images resulted in separation of five different types of porosity (Figure 3): 1) kerogen porosity in the organic mixture domain, 2) pyrite porosity in the pyrite domain, 3) quartz porosity and 4) chalcedone porosity in the matrix domain, 5) large pores visible on many SEM images (e.g., around pyrite or between aggregates of different phases). Figure 3 represents the same sample as Figure 2, but in much larger scale (sample width of 300 µm). Again, after definition of all types of porosity and their spatial distribution on the microscale (microtomography scale) it is clear that only kerogen porosity is connected for Samples 1 and 2, and thus should provide most contribution to permeability and flow. All domains may contain some under-resolution porosity, which potentially can be connected to other types of porosity in a percolating network (Table 1). Total porosity (accounting for the five porosity types) in samples measured by kerosene saturation varies from around 5 to 10%, while kerogen porosity reaches values up to 32% (as measured from SEM images). Combined large porosity and organics mixture domains give a good approximation of total porosity for samples depicted in Figures 2-4, thus providing additional evidence of the dominance of this type of porosity, their overall connectivity and hence their importance to filtration properties.

Similar domain distributions are found in many samples (see Sample 2 in Figure 4). However, for the Sample 3 (Figure 5) the observations were relatively different and segmentation of subdomains was almost impossible. We show only approximate relatively clear phases: matrix and carbonated radiolarians (grey); pyrite globules and crystals (red), clearly visible voids (blue); some porosity between different aggregates probably filled with silica or chalcedony, possessing apparent under-resolution porosity (brown); under-resolution porosity mainly filled with pyrite (green). This particular sample does not have kerogen porosity and its permeability is low (Sample 3 in Table 1).

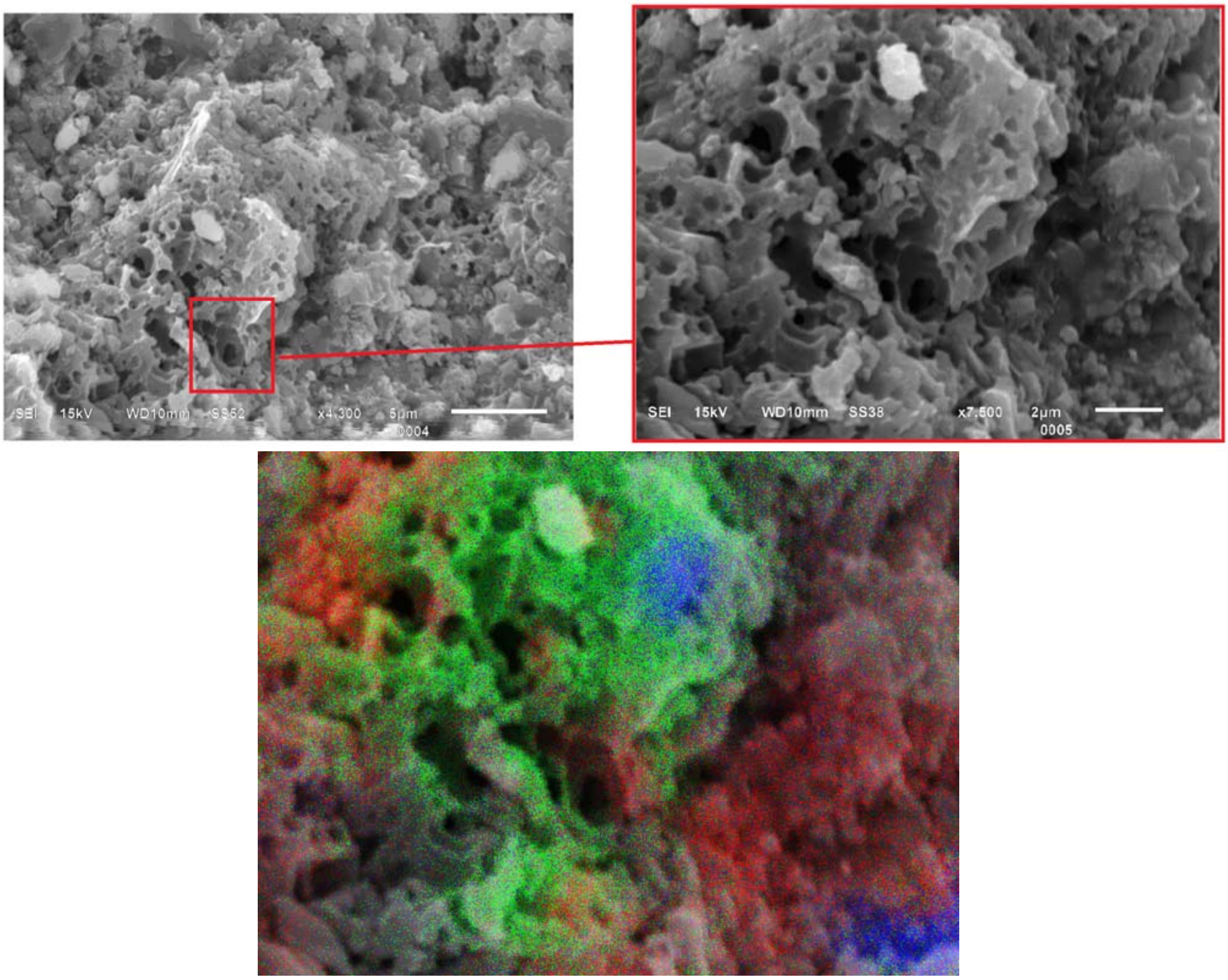

Figure 1. SEM image of Bazhenov shale. Spongy porosity attributed to kerogen imbedded into clay and pyrite matrix shown at different scales (top). Spatial distribution of sulphur (blue), carbon (green) and silicon (red) in same image (bottom).

Figure 6 shows SEM images of kerogen porosity which were segmented and used as input data for stochastic reconstructions. Resulting 3D images were used to extract pore-network models. Examples for 2D cuts on Figure 6 are shown in Figure 7. Depending on the input image, the resulting pore-networks had around three to seven thousand elements (pore bodies and pore throats). All resulting pore-networks were used to simulate gas flow under different pressure conditions, including pressures similar to those used in laboratory measurements. For three 2D cuts (Images 1-3) the following gas permeabilities were obtained (SL_{2xyz} reconstructions which were visually best representing original images): 0.604, 0.57, and 0.52 mD (reported as averages in three principal directions). Reconstructions with correlation functions calculated in the three principal directions did not significantly change simulation results as kerogen porosity is isotropic (Figure 8). Modeled kerogen permeability values are higher than average gas permeability for most samples measured in the lab (Table 1). The main five reasons for this are: 1) kerogen porosity images chosen for reconstruction are very porous and, probably, are not representative samples of average kerogen porosity; 2) kerogen porosity is distributed in the mixture domain (see Figures 2-3) and apparently has lower permeability in comparison with the same sample containing kerogen porosity only; 3) stochastic reconstructions with higher order statistics (cluster functions, three-point statistics, etc.) could probably improve reconstruction results, but this should result in even higher permeability values; 4) other types of porosity can contribute to permeability, especially large voids; 5) laboratory methods can provide incorrect results (Khamidullin et al, 2012). It also very important to mention that depending on the kerogen porosity image, permeability can differ significantly. This means that fast SEM imaging and stochastic reconstructions can be much more useful than FIB-SEM tomography, as the latter is too time consuming and hard to perform in numerous places within samples. Clearly, one way to use pore-scale modeling results is to solve Darcian flow in a mixture domain geometry with distributed permeability values. This means that the amount of statistical information, i.e., different parts of kerogen porosity studied, will significantly improve macro-scale simulations.

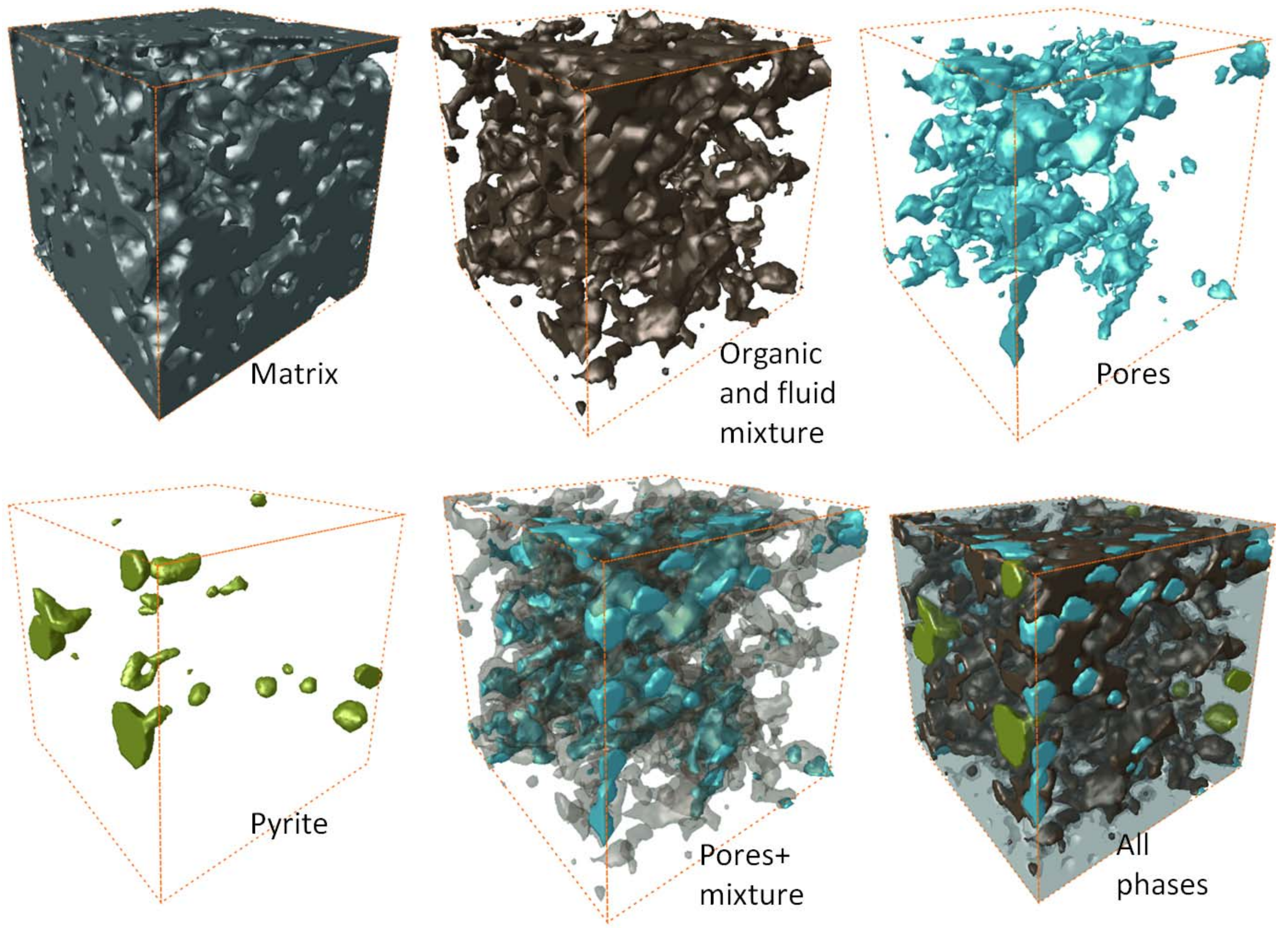

Figure 2. Different domains identified from microtomography images for Sample 1: rock matrix, pores containing a mixture of organics and fluid, pores larger 1 µm mostly containing free hydrocarbons, pyrite, and all phases combined. Width of the cube is 100 µm.

Simulation results for all reconstructions are shown in Figure 8a. Differences at lower pressures are especially pronounced for reconstructions based on Image 3, which has a higher fraction of smaller pores in comparison with Images 1-2. Similar to Mehmani et al. (2013) we also present ratios of permeabilities if simulations would be performed without different physics for nano-porosity (Figure 8b). Differences are especially pronounced for lower pressures and samples with higher amount of small pores.

Finally, we present a framework to obtain physical properties of unconventional reservoir rocks using muti-scale structure information (Figure 9). SEM or FIB-SEM imaging can be used to obtain structural information about different types of porosity (e.g., kerogen, quartz, pyrite, any other specific to the rock under study). FIB-SEM is a technique that provides detailed 3D information about nano-structure, but it is time consuming and cannot be used to mill the same sample in many different locations. SEM imaging is fast and simple and can be easily performed for different locations within a sample, but provides only 2/2.5D information to reconstruct the 3D structure using one of the following methods: stochastic reconstructions (Yeong and Torquato, 1998), process-based (Oren and Bakke, 2003) or germ-grain methods (Biswal et al., 2009). The amount of information obtained using nano-imaging is crucial for the quality of final simulations, as we have shown earlier; effective properties of the same porosity domains within a sample can vary significantly. Based on numerous reconstructions and pore-scale modeling results one can create a statistical model of effective property distribution in space, which can be used later for macro-scale (Darcian scale) simulations. High-resolution X-ray microtomography imaging (still with good sample size-resolution trade-off to obtain representative sample) can be used to assess geometry of large pores and different porosity domains (e.g., kerogen porosity, pyrite porosity, or any other specific to the rock). These two scale results can be combined together to solve Darcian flow equations in 3D geometry of the sample and, thus, upscaling results of nano-pore-scale modeling to obtain effective property specific to the sample under study. At some domains pore-scale modeling results can be improved using a previously developed concept of under-resolution porosity (Korost and Gerke, 2012), which can be used, for example, to combine kerogen, pyrite and other types of nano-porosity and large pores.

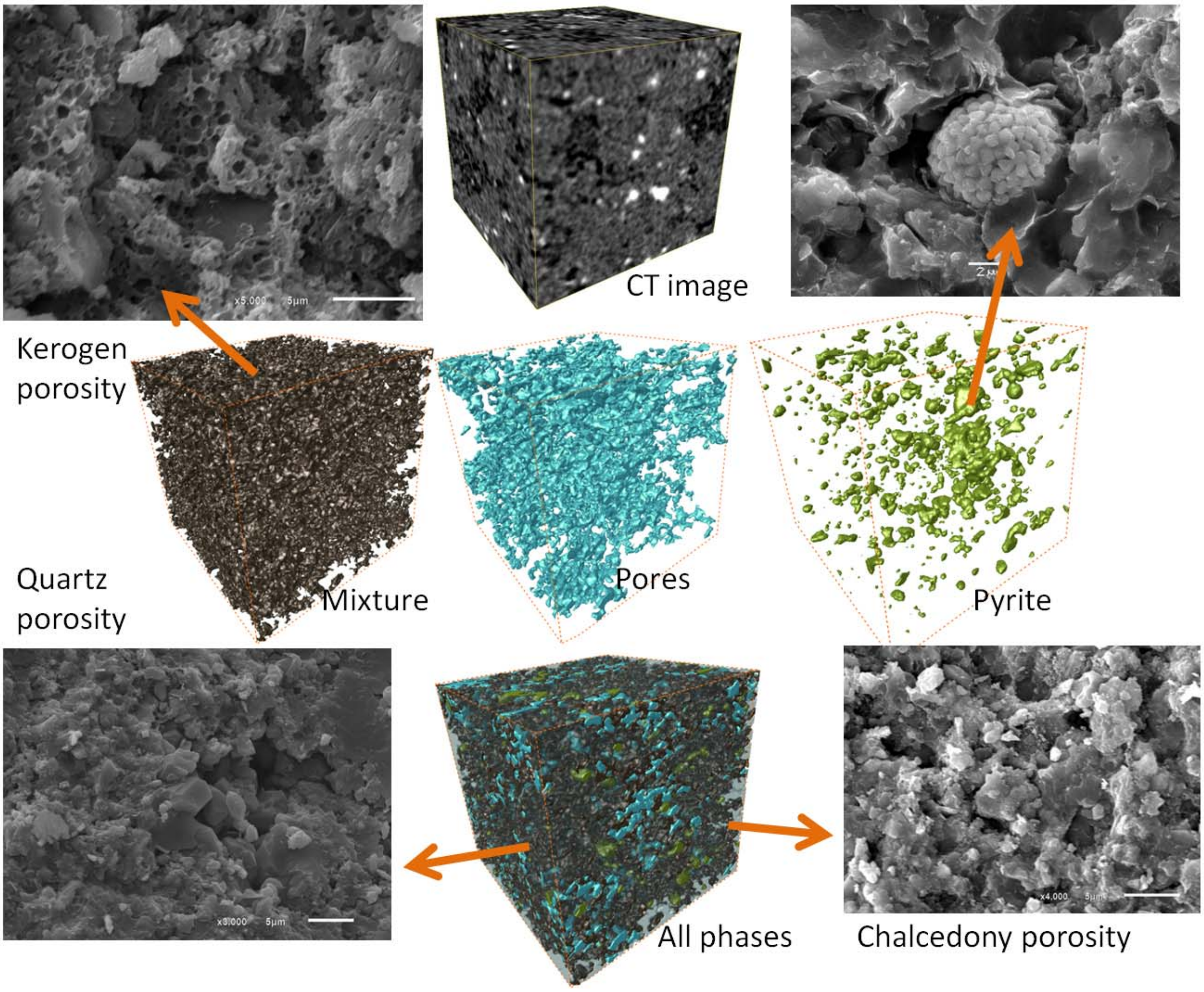

Figure 3. Different phases identified from microtomography images shown together with SEM images of different phases/minerals and their associated porosities (Sample 1). Width of the cube is 300 µm.

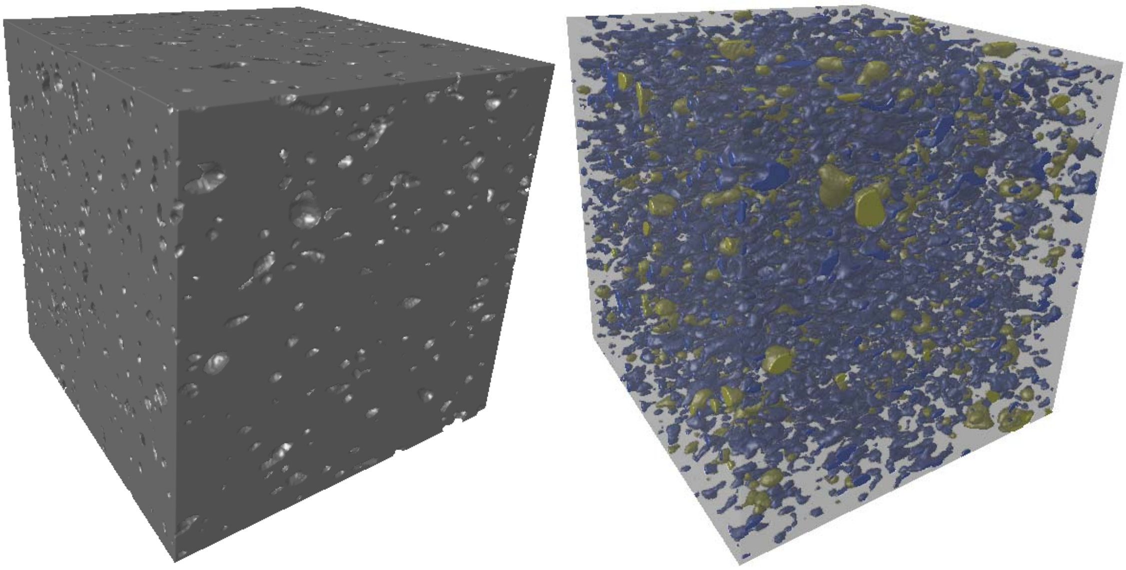

Figure 4. Matrix (left) and pores and pyrite domains (right) (Sample 2). Width of the cube is 300 µm.

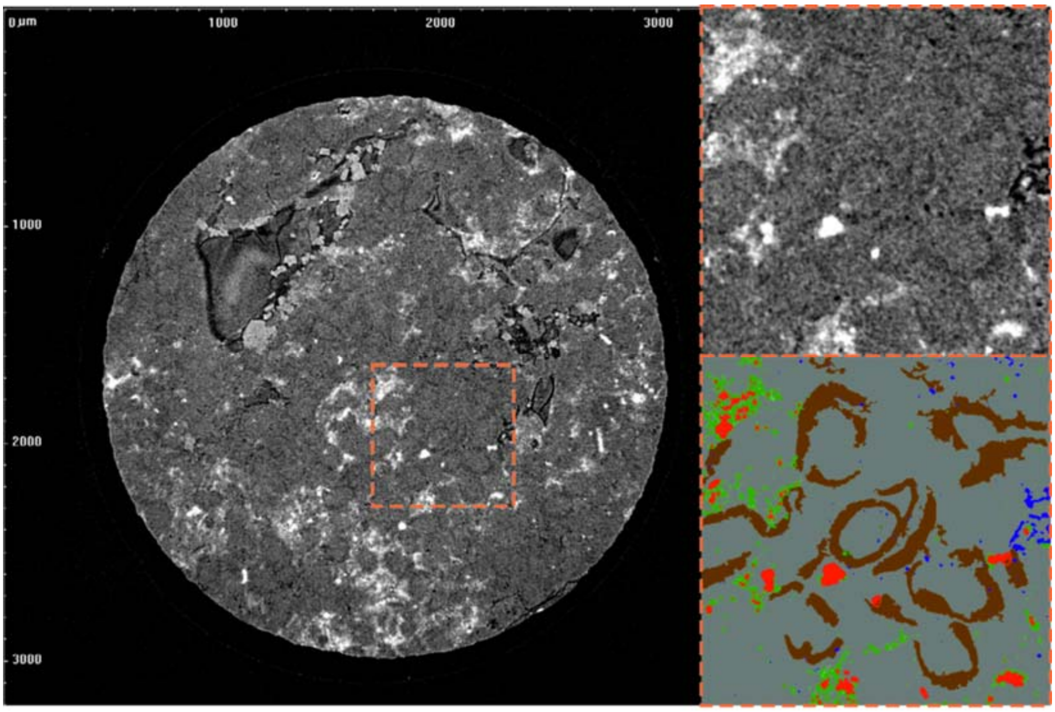

Figure 5. Distributions of different domains (Sample 3): matrix and carbonated radiolarians (grey); pyrite globules and crystals (red), clearly visible voids (blue); some porosity between different aggregates, probably filled with silica or chalcedony, and possessing apparent under-resolution porosity (brown); same as brown, but under-resolution porosity is mainly filled with pyrite (green).

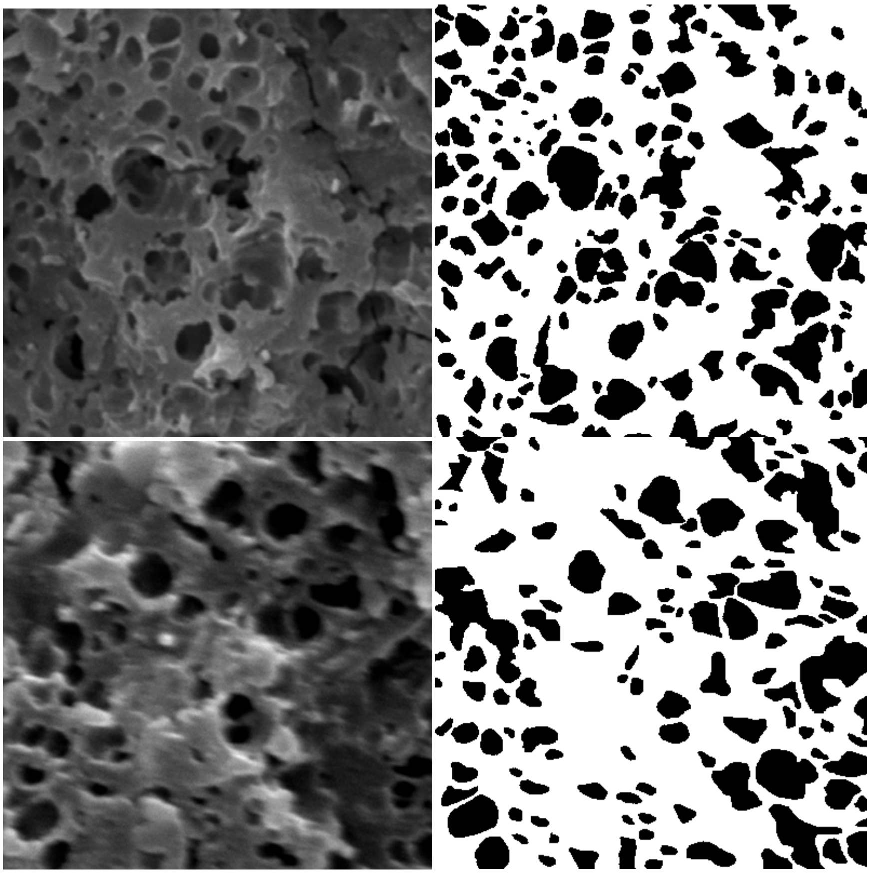

Figure 6. Original SEM and segmented images of kerogen porosity used for 3D stochastic reconstructions (Images 1 and 3). Resolutions for SEM images are 18 and 10 nm, respectively.

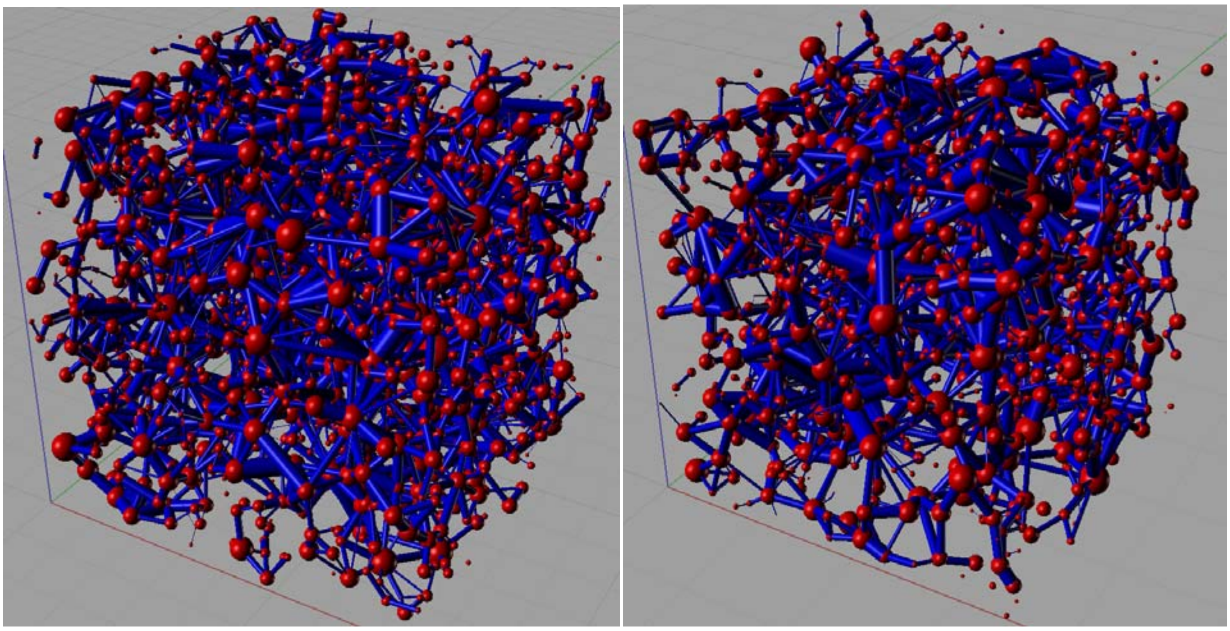

Figure 7. Pore-networks extracted from 3D stochastic reconstructions resulted from 2D cuts shown in Figure 6.

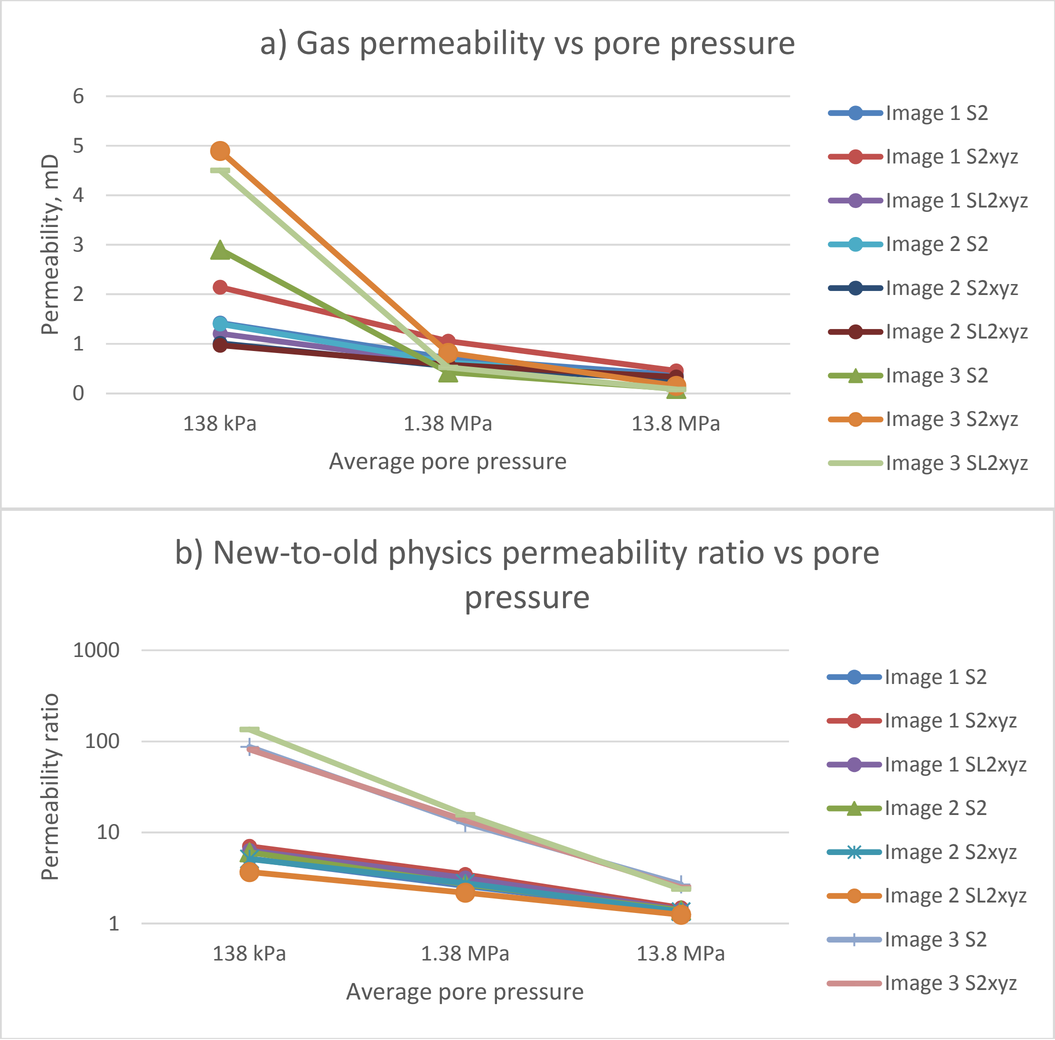

Figure 8. Gas permeability results for all reconstructions.

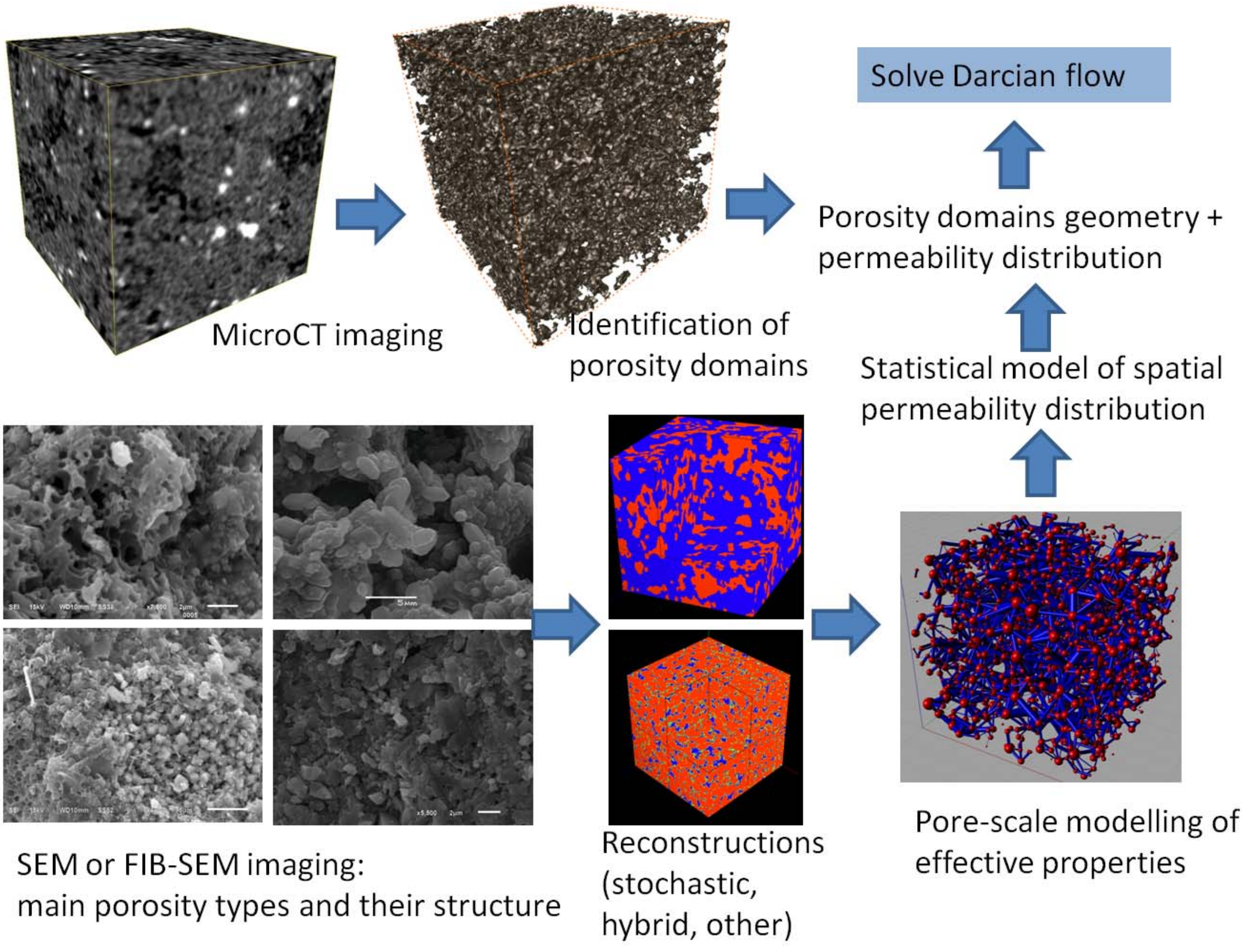

Figure 9. Main framework to combine nano-pore-scale modeling and micro-structure information from microtomography.

Summary

A framework was developed for determining physical properties of unconventional reservoir rocks by combination of modeling and high-resolution imaging. Laboratory measurements involved X-ray microtomography and SEM imaging on more than 20 samples of Bazhenov siliceous rock; stochastic reconstructions of pore networks followed by pore-scale modeling provided estimates of gas permeability. Important results include:

1) Using SEM imaging it was shown that Bazhenov siliceous rock contains significant amount of kerogen porosity.

2) Different porosity types were recognized on nano-scale images and further combined with domains on micro-scale tomography images.

3) Kerogen porosity gas permeabilities were modeled using stochastic reconstructions and a pore-network model with different flow physics for micro and nano-scale pores.

4) Effective properties of porosity types in different locations within samples can vary significantly, so that a single FIB-SEM imaging study cannot be used to obtain a representative nano-scale 3D image.

5) Modeled gas permeability values for kerogen porosity are in a good agreement with independent gas permeabilities measured in the laboratory.

Acknowledgements

We are indebted to Brendan Speet (CSIRO Land and Water) for help with high performance computing resources. We also thank Prof. V.V. Voevodin and Dr. P.A. Bryzgalov for computational resources of Moscow State University Computational Center. This work was partially supported by RFBR grants 12-05-33089, 12-04-32264, 13-04-00409, 13-05-01176 and 12-05-01130.

References

1. Ambrose R.J., Hartman R.C., Diaz-Campos M., Akkutlu I.Y., Sondergeld C.H.. Shale gas-in-place calculations. Part I. New pore-scale considerations. // SPE J. 17(1) (2012), pp. 219–229.

2. B. Biswal, P.E. \Oren, R.J. Held, S. Bakke and R. Hilfer. Modelling of multi-scale porous media. // Image Anal Stereol, 2009;28:23-34.

3. Blunt M.J., Bijeljic B., Dong H., Gharbi O., Iglauer S., Mostaghimi P., Paluszny A., Pentland C.. Pore-scale imaging and modelling. // Advances in Water Resources, Volume 51 (2013), pp.197-216

4. Blunt M.J., Jackson M.D., Piri M., Valvatne P.H. Detailed physics, predictive capabilities and macroscopic consequences for pore-network models of multiphase flow. // Advances in Water Resources 25 (8), 1069-1089.

5. Braduchan Yu.V., Gurari F.G., Zaharov V.A. Bazhenov formation in Western Syberia. // Nauka, Novosibirsk, 216p. (1986) (in Russian).

6. Čapek P., Hejtmánek V., Kolafa J., Brabec L.. Transport Properties of Stochastically Reconstructed Porous Media with Improved Pore Connectivity // Transport in Porous Media, Volume 88, Issue 1 (2011) pp. 87-106

7. Curtis M.E., Amrrose R.J., Sondergeld C.H., Rai C.S.. Structural characterization of gas shales on the macro- and nano-scales. // SPE-137693, CSUG/SPE Canadian Unconventional Resources and International Petroleum Conference (2010) October 19-21, 2010, Calgary, Alberta.

8. Dewers T., Heath J., Ewy R., Duranti L.. Three-dimensional pore networks and transport properties of a shale gas formation determined from focused ion beam serial imaging. // Int. J. Oil Gas Coal Technol. 5(2/3) (2012), pp. 229–248

9. Dong H., Blunt M.J.. Pore-network extraction from micro-computerized-tomography images // Phys. Rev. E 80, 036307 (2009)

10. Kalmykov G.A., Balushkina N.S., Afanasiev I.S., Gavrilova E.V., Birun E.M. Bazhen formation: overview and current problems. // Rosneft bulletin, 2010, 4: 20-25 (in Russian).

11. Khamidullin R.A., Kalmykov G.A., Korost D.V., Balushkina N.S. Bakay A.I. Reservoir properties of the Bazhenov formation. // SPE162094 Technical paper, presented at SPE Russian Oil and Gas Exploration and Production Technical Conference and Exhibition, 16-18 October 2012, Moscow, Russia.

12. Korost D.V., Gerke K.M. Computation of reservoir properties based on 3D-structure of porous media. // SPE 162023 Technical paper, presented at SPE Russian Oil and Gas Exploration and Production Technical Conference and Exhibition, 16-18 October 2012, Moscow, Russia.

13. Loucks R.G., Reed R.M., Ruppel S.C., Jarvie D.M.. Morphology, genesis, and distribution of nanometer-scale pores in siliceous mudstones of the Missisipian Barnett Shale// Journal of Sedimentary Research, 79 (2009), pp. 848-861.

14. Mason, G. and Morrow, N.R. Capillary Behavior of a Perfectly Wetting Liquid In Irregular Triangular Tubes,// J. Coll. Inter. Sci., 1991,141: 262-274.

15. Mehmani A., Prodanović M., Javadpour F.. Multiscale, Multiphysics Network Modeling of Shale Matrix Gas Flows // Transp Porous Med, DOI 10.1007/s11242-013-0191-5 (2013)

16. Oh W., Lindquist B. Image thresholding by indicator kriging. // 1999, IEEE Trans. Pattern. Anal. Mach. Intell, 21: 590-602.

17. Øren P., Bakke S., Reconstruction of Berea Sandstone and Pore-Scale Modeling of Wettability Effects // Journal of Petroleum Science and Engineering, 2002, 39: 177-199.

18. Patzek T.W., and Silin D. B., Shape factor and hydraulic conductance in noncircular capillaries I. One-phase creeping flow // Journal of Colloid and Interface Science, 236, 295-304, 2001.

19. Sergeev Y.M., Spivak G.V., Sasov A.Y., Osipov V.I., Sokolov V.N.,Rau E.I. Quantitative morphological analysis in a SEM-microcomputer system-I. Quantitative shape analysis of single objects. // Journal of Microscopy, 1984, 135: 13-25.

20. Silin D., Patzek T.. Pore space morphology analysis using maximal inscribed spheres // Physica A: Statistical Mechanics and its Applications, Volume 371, Issue 2, 15 (2006), pp. 336–360

21. Torquato S.. Random heterogeneous materials: microstructure and macroscopic properties // Springer, 701 p. (2002)

22. Valvante P.H., and. Blunt M.J. Predictive pore-scale modelling of two-phase flow in mixed wet media. // Water Resources Research, 40, W07406, doi: 10.1023/2003 WR002627. 2004.

23. Yeong C.L.Y., Torquato S.. Reconstructing random media: II. Three-dimensional media from two-dimensional cuts. // Physical Review E 58 (1) (1998), pp. 224–233.